



Ductile fracture based joint formation mechanism during friction stir welding

Nakul D. Ghate, Aarush Sood, Avijit Srivastava, Amber Shrivastava*

Indian Institute of Technology Bombay, Mumbai, MH, India



ARTICLE INFO

Keywords:

Friction stir welding
Plastic limit load model
Joint formation mechanism
Material flow

ABSTRACT

Material movement during friction stir welding plays a significant role towards joint formation. However, there is little clarity on periodic or continuous nature of material movement. The objective of this work is to understand the mechanism of joint formation during friction stir welding, by investigating the periodic formation of a cavity and if formed, cavity's role towards the joint formation. A two dimensional numerical methodology is developed to capture the material flow around the tool pin. The plastic limit load model is used to predict the formation of microvoids, growth and coalescence. Friction stir welds are made with AA 1050 at different tool travel speeds, for same tool rotation frequency across experiments. Computed tomography of friction stir welded samples is performed to study the size and morphology of the discontinuities. The chemical constituents, size and distance between inclusions are determined from scanning electron microscopy and energy dispersive spectroscopy of the as-received AA 1050. The numerical model suggests that the stress and strain during friction stir welding of AA 1050 is sufficient for nucleation and growth of the voids at the inclusion sites. Further the voids coalesce to form a cavity in all the cases. The incoming material fills the cavity per revolution. However, in some cases the cavity is partially filled which leads to the discontinuities in the weld. For the welds with discontinuities, the area of unfilled cavity is predicted to be larger in advancing side as compared to retreating side. The discontinuity size increases as the travel speed increases. The tunnel discontinuity is predicted by super-positioning of the discontinuities formed over consecutive passes along the feed direction. The discontinuity size and shape trends compare well against the experimental observations. This work would be helpful towards developing strategies for detecting and mitigating the discontinuities formed during friction stir welding.

1. Introduction

Friction stir welding (FSW) is a solid state joining process [1]. This process involves a non-consumable friction stir (FS) tool, which generally consists of a pin and a shoulder. Fig. 1 shows a schematic of the FSW process. During FSW, the rotating FS tool is plunged into the workpiece and travelled along the weld line, under an axially compressive load. This results in severe plastic deformation around the tool pin and below the shoulder [2]. The plastically deformed material from the workpieces mixes under the influence of FS tool, which leads to the joint formation. The workpiece material(s) does not melt during the process. This leads to several advantages over conventional fusion welding techniques like, lower thermal distortion, lower residual stresses, lower energy consumption, no filler material, no fumes etc. [3]. There have been numerous experimental and numerical efforts to understand the joint formation mechanism during FSW. The material flow during FSW is fundamental to the joint formation [4]. Some of the early work [2,5] showed that the material in the weld zone extrudes continuously around the

retreating side (RS) of the FS tool pin, as the material moves from the leading side to the trailing side. Based on FSW of 4 mm thick aluminum 2017-T4 and plasticine plates, Gratecap et al. [6] suggested two separate material flow patterns: one under shoulder and other around pin. Based on post-weld observations, Kumar et al. [7] proposed that the pin transfers material layer by layer (discontinuously), while the shoulder continuously transfers material around the FS tool. Further, authors concluded that fully consolidated joints are formed when pin driven material merges with the shoulder driven flow. The discontinuities are formed when material doesn't reach advancing side (AS). Many studies [8–11] have reported that the forces oscillate at FS tool rotation frequency during FSW. However, there is no consensus on the origin of the force oscillations. Some researchers [12,13] suggest that the FS tool pin runout leads to the force oscillations, while others have proposed that the force oscillations are due to the discontinuous material flow (layer by layer) around the FS tool pin [14–16]. Based on the post-weld observations, Li et al. [17] proposed that the material is sheared in front of the rotating pin and extruded back from the RS. Once per FS tool revolution, a temporary cavity forms at the AS and the plasticized material is extruded into the cavity and fills it. Shrivastava et al. [18] studied the discontinuities formed during FSW and suggested that the discontinuities

* Corresponding author.

Nomenclature

$A, B, C, m \& n$	Johnson–Cook parameters
c_p	specific heat (J/K)
f	fraction of heat generated available to workpiece
H_p	tool pin height (mm)
N	tool rotation frequency (rev/min)
q_{gen}	heat generated per unit volume (J/mm ³)
ρ	density (kg/m ³)
C_p	specific heat capacity (J/kg-K)
k	thermal conductivity (W/m ²)
R_p	tool pin radius (mm)
R_0	inclusion size (μm)
R_s	tool shoulder radius (mm)
\dot{R}_x	rate of void size change ($\mu\text{m}/\text{s}$)
v_{max}	velocity at the tool-workpiece periphery
$v_t(r)$	tangential velocity as a function of radial distance (r)
T	temperature (K)
V_T	tool travel speed (m/s)
ρ	density (kg/m ³)
u	velocity component along x-direction (m/s)
v	velocity component along x-direction (m/s)
ω	tool angular velocity (rad/s)
ε_{eq}	equivalent strain [-]
ε_i	principal strains [-]
ε_k	strain [-], $k = x, y, xy$
$\dot{\varepsilon}_{eq}$	equivalent strain rate (s ⁻¹)
$\dot{\varepsilon}_i$	principal strain rates (s ⁻¹), $i = 1, 2$
\dot{R}_x	strain rate (s ⁻¹), $k = x, y, xy$
σ_k	stress (Pa), $k = x, y, z$
σ_i	principal stresses (Pa), $i = 1, 2$
$\bar{\sigma}$	flow stress (Pa)
σ_c	critical decohesion stress (Pa)
σ_{loc}	local stress (Pa)
σ_m	mean normal stress (Pa)
σ_{rr}	interfacial stress (Pa)
σ_{yield}	yield strength (Pa)
λ	plastic multiplier
v	lode parameter
W_p	workpiece
T_l	tool
R_{mean}	mean void size (mm)
$Area_{in_i}$	area inflow at layer ' i ' (mm ²)
$Area_{cav_i}$	area of cavity formed at layer ' i ' (mm ²)
APR	advance per revolution (mm/rev)
AS	advancing side
CT	compute tomography
EDS	energy dispersive spectroscopy
FSW	friction stir welding
ipd	inter-particle distance (μm)
RS	retreating side
SEM	scanning electron microscopy
CFD	computational fluid dynamics
CSM	continuum solid mechanics
FSI	fluid-solid interaction model

nancies are formed due to incomplete filling of the cavity, which opens once per revolution at the trailing edge of the FS tool. The direct experimental observation of the material flow around FS tool pin is very difficult, as the stir zone is completely enclosed during the process (FS tool from top, base material from sides and backing plate from bottom, Fig. 1).

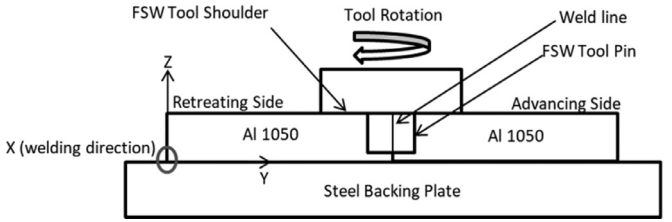


Fig. 1. Schematic of the FSW process.

Over last two decades, various numerical studies have been performed to capture the material flow. He et al. [19] performed exhaustive review of the numerical analysis of FSW. These efforts utilize computational fluid dynamics (CFD) based models [1,20–22], computational solid mechanics (CSM) based models [23,24] or smooth particle hydrodynamics based models [25] to solve the coupled thermo-mechanical equations [26–28] and predict the temperature field, strain field & strain rate field to visualize the material flow during FSW. Different meshing schemes like Eulerian [29–31], Lagrangian [32,33], Arbitrary Lagrangian Eulerian [34,35] have been attempted to improve the solution accuracy and time efficiency. Simar et al. [36] developed an integrated model (thermal model coupled with microstructure evolution model) to predict the yield strength, ultimate tensile strength and elongation for friction stir welds of Al 6xxx series alloys. Huang et al. [37,38] used fluid-solid interface method to study the joint formation during high depth-to-width ratio FSW of Al-Mg-Si. Tutuncilar et al. [39] developed a Lagrangian incremental finite element model for simulating the friction stir processing (FSP) of Al-Si cast alloy and reported loss of contact between the tool and workpiece due to negative pressure at the interface. Heurtier et al. [40] developed a semi analytical three-dimensional (3D) thermo-mechanical model to estimate the strains, strain rates, temperatures and resulting micro-hardness. Cho et al. [41] developed a steady state 3D thermo-mechanical model with viscoplastic self-consistent approach to capture the microstructural texture development during FSW of ferritic stainless steel. Bastier et al. [42] used an elastoviscoplastic constitutive law in conjunction with a CFD based model to capture the residual stresses induced from FSW of Al 7050 alloy. These models offer interesting insights into the material movement, associated microstructural evolution and resulting joint properties. However, with these models, it would be very difficult to capture any periodicity in material flow around FS tool pin, as indicated by some of the experimental works previously. This is because fracture criterions are not employed to explore the possibility of a cavity formation in stir zone, due to nucleation of microvoids, followed by growth and coalescence of the voids, if formed.

Ductile fracture criteria are successfully implemented in the past for sheet metal forming [43], deep drawing [44], and hot deformation [45]. However, to the author's knowledge, a ductile fracture based approach is not attempted previously for FSW, to investigate the formation of voids, their growth and coalescence, which could result in a cavity. The prior research work shows that the joint is created by in-situ extrusion of material around the FS tool during friction stir welding. However, it is not evident if a cavity is formed once per revolution at the trailing edge of the FS tool. The objective of this work is to understand the mechanism of joint formation, by investigating the periodic formation of a cavity and if formed, cavity's role towards the joint formation during FSW. This work will improve the current understanding of material flow and the mechanisms which lead to the formation of discontinuities (i.e., voids) in the friction stir welds.

2. Numerical methodology

A numerical methodology is developed to analyze the formation of cavity and its role towards the joint formation during FSW. The material

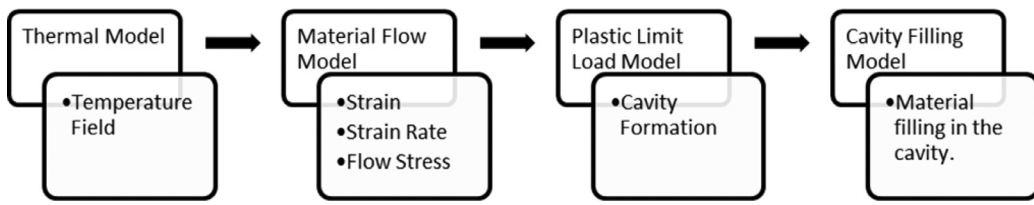


Fig. 2. Flow chart showing the implementation sequence of the models.

flow around the FS tool pin is considered in this study. Fig. 2 shows the sequence of the mathematical models. These mathematical models are discussed in the sub-sections below.

2.1. Thermal model

There have been many attempts (experimental as well as numerical) to capture the temperature profile during FSW/FSP for different materials and FS tool designs. One common take away from these studies is that the temperature of shoulder driven material is more than the pin driven material [19–22,24–26,28,29,31,32,36–42,46]. However, the temperature variation within pin driven region is primarily in radial direction for FS tools with cylindrical and tapered pins [21,28,30,32,36,40,41]. Two-dimensional steady-state energy conservation equation (Eq. (1)) is solved to estimate the temperature distribution around the FS tool pin, in the stir zone. Eq. (1) is discretized with grid spacing equal to inter-particle distance (*ipd*) between inclusions (Section 4.1) and solved explicitly.

$$k \frac{\partial^2 T}{\partial x^2} + \frac{\partial^2 T}{\partial y^2} + q_{gen} = 0 \quad (1)$$

where, k is the thermal conductivity of the material, T is the temperature and q_{gen} is the heat available to the workpiece, given by Eq. (2) [32].

$$q_{gen} = f \frac{2}{3} \frac{\sigma_{yield}}{\sqrt{3}} \omega [(R_s^3 - R_p^3) + R_p^3 + 3R_p^2 H_p] \quad (2)$$

Here, σ_{yield} is the yield strength of the material, R_s is the shoulder radius, R_p is the pin radius, ω is the angular velocity of the FS tool, H_p is the FS tool pin height and f is the fraction of total heat generated [22], which is available to (carried away by) the workpiece.

$$f = \sqrt{(k\rho c_p)_{Wp}} / \sqrt{(k\rho c_p)_{Tl}} \quad (3)$$

where ρ and c_p stand for density and specific heat capacity respectively. Here 'Wp' stands for workpiece and 'Tl' stands for FS tool.

2.2. Pin-driven material flow model

As discussed in Section 2.1, in pin driven region, temperature primarily varies in radial direction. Further a no slip [1–3,20–22,31,35,36] or a constant slip [30,32,34,37–39] at FS tool pin-material interface (including thickness direction) would lead to minimal change in velocity, strain and stress fields along the thickness direction [30,32,34,37–39], under pin's effect alone on the pin driven material [5]. This work focuses on the periodicity of material flow, which is particular to the pin driven region [5,7–10]. Therefore a simple two-dimensional model is developed for pin driven material which considers the material flow around pin, only under the influence of pin, with following assumptions: sticking condition between FS tool pin periphery and material; width of stir zone in the radial direction is same as the advance per revolution ($APR =$ feed rate/FS tool rotation frequency); the tangential velocity in the stir zone decreases linearly along the radial direction (from v_{max} at the FS tool pin periphery to zero at the stir zone outer periphery). The tangential velocity, v_r in the stir zone is given by,

$$v_r(r) = v_{max} - C(r - R_p) \quad (4)$$

where, $C = v_{max}/APR$ and $v_{max} = \omega R_p$ is the tangential velocity at FS tool pin periphery. The tangential velocity $v_r(r)$ is resolved into u (x-component) and v (y-component).

$$u = v_r \sin \theta \quad (5)$$

$$v = v_r \cos \theta + V_T \quad (6)$$

Here, θ is the angle from the positive abscissa, assuming tool center at origin. V_T is the travel speed of the FS tool. The strain rates in the workpiece are given by:

$$\dot{\epsilon}_x = \frac{\partial u}{\partial x} \quad (7)$$

$$\dot{\epsilon}_y = \frac{\partial v}{\partial y} \quad (8)$$

$$\dot{\epsilon}_{xy} = \frac{1}{2} \left(\frac{\partial u}{\partial y} + \frac{\partial v}{\partial x} \right) \quad (9)$$

The forward space finite difference approach is used to discretize the Eqs. (7)–(9) at each grid point to compute the strain rate components. Strain is calculated by multiplying strain rate with dt , where dt is the time for which particular inclusion is exposed to the stress field. The time, dt was considered to be $60/N$ where N is the FS tool rotation frequency in rev/min. The Johnson–Cook constitutive model [47] is used to account for the effects of strain, strain rate and temperature on the von Mises flow stress (Eq. (10)).

$$\bar{\sigma} = [A + B \epsilon_{eq}^{n1}] [1 + C \ln \dot{\epsilon}^*] [1 - T^{*m}] \quad (10)$$

It makes use of the equivalent strain rate, $\dot{\epsilon}_{eq}$ and strain, ϵ_{eq} calculated as,

$$\epsilon_{eq} = \sqrt{\frac{2}{3} (\dot{\epsilon}_x^2 + \dot{\epsilon}_y^2 + 2\dot{\epsilon}_{xy}^2 - \dot{\epsilon}_x \dot{\epsilon}_y)} \quad (11)$$

$$\dot{\epsilon}_{eq} = \dot{\epsilon}_{eq} dt \quad (12)$$

where, $\dot{\epsilon}^* = \dot{\epsilon}_{eq}/\dot{\epsilon}_0$ is the dimensionless equivalent plastic strain rate for a reference strain rate $\dot{\epsilon}_0$ and $T^* = (T - T_{room})/(T_{melt} - T_{room})$. The melting temperature of AA 1050 is taken as 903 K [57], the room temperature T_{room} is taken as 300 K and the reference strain rate is taken as 1 s^{-1} . Table 1 shows the values of the Johnson–Cook parameters for AA 1050.

2.4. Plastic limit load model

Under sufficient stress/strain, microvoids tend to nucleate at the sites of inclusions and second phase particles in a plastically deformed metal matrix. For the particle size $\sim 1 \mu\text{m}$, continuum plastic models are required to describe the microvoid nucleation process [49,50]. The second phase particles and inclusions can vary in shapes from spherical to lamellar or irregular [51]. However, for simplicity, spherical voids are assumed in this work. For Al alloys, a critical stress based criteria well captures the nucleation of microvoids due to inclusions of size $\sim 0.5 - 1.1 \mu\text{m}$ present in the material [52,53]. For as-received AA 1050, the average inclusion size of $0.7 \mu\text{m}$ and the average inter-particle distance

Table 1
Johnson–Cook model parameters for AA 1050 [48].

Parameters	A	B	C	m	n
Value (units)	67.456 (MPa)	471.21 (MPa)	0.002979	2.5186	0.4241

Table 2
Material properties of AA 1050.

Material properties (AA 1050)	Value (units)
Density (ρ_{WP})	2710 (Kg/m ³) [66]
Specific heat capacity ($C_{p_{WP}}$)	900 (J/Kg) [66]
Thermal conductivity (kWp)	222 (W/m–K) [66]
Melting temperature (T _{mel})	903 K [57]
Reference temperature (T _{room})	300 K
Young's modulus (Y)	70 (GPa) [59]
Yield stress (σ_{yield})	110 (MPa) [59]
Shear modulus (μ)	26 (GPa) [60]
Parametric constant (α)	0.2
Burger's vector (b)	0.289 (nm) [61]
Initial void size (R ₀)	0.4–0.7 (μm) [53]
Inter-particle distance (ipd)	5.3 (μm) (Fig. 5(a))
Void decohesion strength (σ_c)	550 (MPa) [62]

of 5.3 μm is observed (Section 4.1). The interfacial stress between the inclusion and matrix interface σ_{rr} is given as [52]:

$$\sigma_{rr} = \sigma_{loc} + \sigma_m \quad (13)$$

$$\sigma_{loc} = 5.4\mu\alpha\sqrt{\frac{\epsilon_p b}{R_0}} \quad (14)$$

Where, σ_{loc} is the local stress field and σ_m is the mean normal stress ($\sigma_m = \sigma_{ii}/3$). The mean normal stress is calculated using the principal strains as follows:

$$\begin{aligned} \dot{\epsilon}_1 &= \frac{1}{2}(\dot{\epsilon}_x + \dot{\epsilon}_y) + \sqrt{\left(\frac{1}{2}(\dot{\epsilon}_x - \dot{\epsilon}_y)\right)^2 + \left(\frac{1}{2}\dot{\epsilon}_{xy}\right)^2}; \dot{\epsilon}_2 \\ &= \frac{1}{2}(\dot{\epsilon}_x + \dot{\epsilon}_y) - \sqrt{\left(\frac{1}{2}(\dot{\epsilon}_x - \dot{\epsilon}_y)\right)^2 + \left(\frac{1}{2}\dot{\epsilon}_{xy}\right)^2} \end{aligned} \quad (15)$$

$$d\epsilon_1 = d\lambda\left(\sigma_1 - \frac{\sigma_2 + \sigma_3}{2}\right); d\epsilon_2 = d\lambda\left(\sigma_2 - \frac{\sigma_1 + \sigma_3}{2}\right); d\epsilon_3 = d\lambda\left(\sigma_3 - \frac{\sigma_1 + \sigma_2}{2}\right) \quad (16)$$

where for plane strain, $d\epsilon_3 = 0$; $\sigma_3 = \frac{\sigma_1 + \sigma_2}{2}$. Here μ is the shear modulus of the material, α is a parametric constant which is usually in the range 0.15–0.35, ϵ_p is the principal strain, b is the burger's vector and R_0 is the initial void size [Table 2]. $d\lambda = \epsilon_p/\bar{\sigma}$ is the plastic multiplier, where $\bar{\sigma}$ is the flow stress and ϵ_p is the equivalent principal strain given by $\epsilon_p = \sqrt{\frac{2}{3}(\epsilon_1^2 + \epsilon_2^2)}$. Integrating Eq. (16) and solving for principal stresses we get

$$\sigma_1 = \sqrt{\frac{2}{3}\left(\frac{2\epsilon_1 + \epsilon_2}{\lambda}\right)}; \sigma_2 = \sqrt{\frac{2}{3}\left(\frac{\epsilon_1 + 2\epsilon_2}{\lambda}\right)} \quad (17)$$

$$\sigma_m = \frac{1}{3}(\sigma_1 + \sigma_2) \quad (18)$$

In continuum plasticity model, for relatively large particles of approximately spherical form, Argon et al. [54,55] suggested a modified σ_{rr} for microvoid nucleation, where flow stress, $\bar{\sigma}$ is included as shown by Eq. (20). This ensures that the solutions to the interfacial (inclusion-matrix) stress (under strain hardening) are bounded by the known solutions for non-hardening materials and purely elastic materials (Eq. (19)) [50,56]. The flow stress is estimated by Johnson–Cook constitutive model [47].

$$1.5\bar{\sigma} + \sigma_m \leq \sigma_{rr} \leq 2\bar{\sigma} + \sigma_m \quad (19)$$

$$\sigma_{rr} = \sigma_{loc} + \bar{\sigma} + \sigma_m \quad (20)$$

Microvoids nucleate when the interfacial stress becomes greater than the critical decohesion stress for the material (σ_c) i.e. $\sigma_{rr} > \sigma_c$. Under continuous loading, microvoids grow in size. In this study, the void growth model of Rice and Tracey [57] is used. Assuming the nucleated microvoids to be spherical, the rate of change of the size of the voids (\dot{R}_x) in the direction 1, 2 of the principal strain rates respectively,

$$= \left\{ (1+E)\dot{\epsilon}_x + \left(\frac{2}{3}\dot{\epsilon}_L\dot{\epsilon}_L\right)^{1/2} D \right\} R_0 \quad (21)$$

where, ($x, L = 1, 2$ and R_0 is the initial size of the void, $(1+E)$ is 5/3 for linear hardening; is 2 for high values of mean normal stress with non-hardening, and $D = 0.588 \sinh(\frac{3\sigma_m}{2\sigma}) + 0.008v\cosh(\frac{3\sigma_m}{2\sigma})$ for non-hardening [55]. Eq. (21) is integrated w.r.t. time till steady state for maximum growth ($t \rightarrow \infty$) to determine the principal radii across the three directions. The mean radius of the void upon growth is given by [55],

$$R_{mean} = \exp\left[\left(\frac{2\sqrt{3+v^2}}{3+v}\right)D\epsilon_1\right]R_0 \quad (22)$$

where, $v = 3\dot{\epsilon}_2/(\dot{\epsilon}_1 - \dot{\epsilon}_3)$ is the lode parameter [52,58], and ϵ_1 is the logarithmic principal strain ($\epsilon_1 = \log(1+\epsilon_1)$) where ϵ_1 is the maximum principal strain. The material properties of AA 1050 are shown in Table 2. Upon sufficient growth, voids contact with neighboring voids and coalesce to form the cavity.

2.5. Two-dimensional cavity filling model

The voids with size $> ipd/2$ (half of the interparticle distance) coalesce and form a cavity. The incoming material distributes/moves over the cavity predicted by the previous model. The stir zone is discretized into concentric rings of width same as the ipd . This divides the cavity and material present in the stir zone into the rings. The velocity of the incoming material into each ring at the leading edge is determined in accordance with Eq. (4). As the tangential velocity (v_r) of the incoming material reduces linearly in radial direction, from v_{max} at FS tool pin periphery to zero at the stir zone outer periphery, the amount of material inflow in the outer rings decrease. The area of incoming material per revolution into i^{th} ring, $Area_{in_i}$ (at radius r from the FS tool center) is given by Eq. (23). The total area of cavity present in the i^{th} ring, $Area_{cav_i}$ is given by Eq. (24). $Area_{in_i}$ and $Area_{cav_i}$ are compared and the incoming material is distributed as shown in Fig. 3.

$$Area_{in_i} = ipdV_rN/60 \quad (23)$$

$$Area_{cav_i} = \sum_j \pi R_{ij}^2 \quad (24)$$

3. Experimental methods

Bead-on-plate friction stir welds of length 100 mm were made on 4 mm thick AA 1050 plates using a commercial vertical milling center (VMC Hardinge 600-II). The FS tool is made up of hardened H13 tool steel with shoulder diameter of 15 mm, cylindrical pin diameter of 5 mm and pin height of 3.4 mm. The tilt angle between FS tool and the workpiece is zero degree. The tool rotation frequency of 1000 rpm and plunge depth of 0.2 mm is kept constant across the welds. A stainless steel backing plate of thickness 1 mm was used during the welds. The friction stir welds were performed with different feed rates to vary the

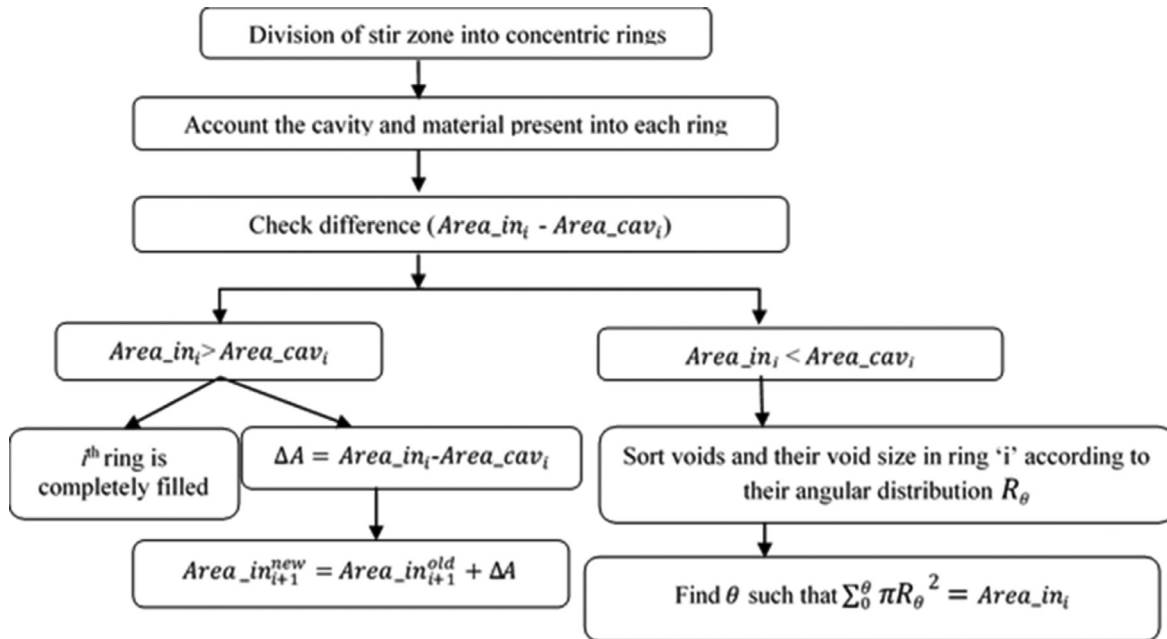


Fig. 3. 2D Cavity filling model.

Table 3
FS tool dimensions and process variables during FSW.

Tool properties and process variables	Value (units)
Pin radius (Rp)	2.5 (mm)
Shoulder radius (Rs)	7.5 (mm)
Pin height (Hp)	3.4 (mm)
Rotational speed (N)	1000 (RPM)
Traverse speed (V _T)	50, 200, 400, 600, 800, 1000 (mm/min)
Tool density (ρ_T)	15,630 (Kg/m ³)
Tool specific heat (C_{p_T})	280 (J/Kg-K)
Tool thermal conductivity (k_T)	85 (W/m-K)

APR, as shown in Table 3. For each value of APR, three welds were performed.

Samples were prepared for metallography by cross-sectioning the friction stir welds. The samples were polished and etched by Keller's reagent. Further, scanning electron microscopy (SEM) and energy dispersive spectroscopy (EDS) of the as-received AA 1050 was done to characterize the type of inclusions, average size and distribution in the base material (AA 1050). Post weld X-ray computed tomography (CT) scan was performed for 20 mm × 20 mm × 4 mm specimens with a commercial X-Ray CT Set-up. The current, voltage and exposure time settings of 100 μA, 130 kV and 20 ms were used for X-ray CT. A voxel size of 75.6 μm is achieved with the CT settings. The 3D dataset was analyzed using Visual Studio software package (Table 4).

4. Results

4.1. SEM and EDS results

Figs. 4 and 5 show the SEM and EDS of as received AA 1050, respectively. EDS revealed Aluminum, Iron and Oxygen in the sample. The inclusions contain mostly the intermetallic compounds of Fe and Si [63]. These were confirmed with the EDS scan over the inclusion (Fig. 5). The average inclusion size of 0.7 μm and the average distance between two inclusions (inter-particle distance, ipd) of 5.3 μm were measured from the SEM results. These results are used in the numerical model (Section 2.1).

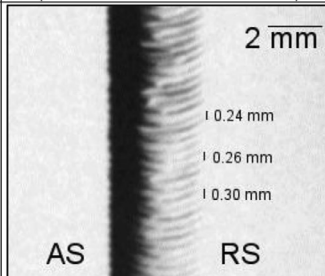
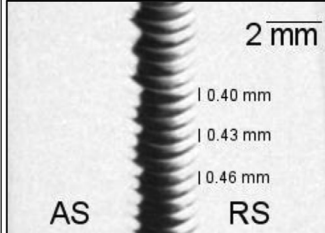
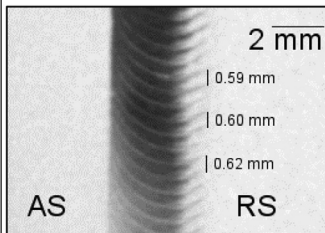
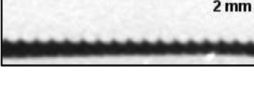
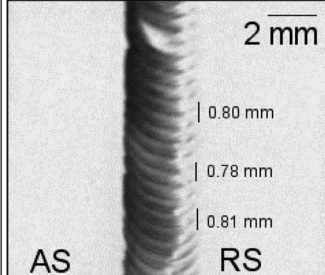
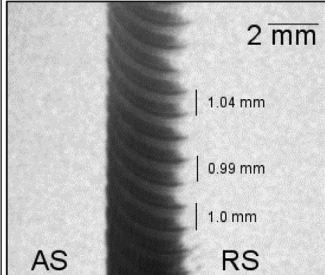
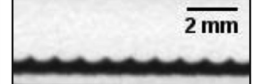
4.2. X-Ray computed tomography results

The X-ray CT images of the friction stir welds are shown in Table 4. CT scans reveal the discontinuities formed in the friction stir welds. In general, for all the welds (except weld at APR = 0.05 mm/rev), the discontinuities are shaped like stack of arcs. The geometry of the discontinuities provides interesting insights into the weld formation mechanism. The distance between two consecutive arcs is observed to be comparable to the theoretical APR (Table 4). The material in these consecutive discontinuities can be seen as a thin lamella. These lamellas are the well-defined arcs with the center towards tool traverse direction. This is due to the direct contact between the material and the FS tool pin. These observations strongly indicate the movement of lamellar material around the FS tool pin once per revolution. The well-defined discontinuities are present regularly (once per revolution) throughout the trailing edge up to the advancing side. The discontinuities tend to form a continuous trench or tunnel discontinuity in the advancing side. This is possibly due to material lamella being not completely squeezed or pushed all the way to the advancing side. This suggests that the cavity is opened during the process and material lamella was pushed into the cavity, as proposed by [2,5]. Most of the lamellas have well-defined arc at their concave side and relatively irregular arc at their convex side. This can be particularly observed from weld 3 (Table 4). This is due to the direct contact between the material and the FS tool pin at the concave side of the lamella. This observation is similar to [7], who proposed that FS tool pin transfers material layer by layer. So it is observed that material is filled effectively in the vicinity of FS tool pin, as compared against the region towards the outer periphery of the cavity. This suggests that the velocity of incoming material decreases from maximum at FS tool periphery to zero at region towards the outer periphery of the cavity. A CT scan was also performed for APR = 0.05 mm/rev. This weld was performed with weld parameters known to produce a fully consolidated weld. This CT scan did not reveal any discontinuities.

Fig. 6 shows the u and v velocity (along x and y directions, respectively) contours in the stir region, for representative APR of 1 mm/rev. The u velocity components range from -207 to 263 mm/s and the v velocity components range from -228 to 228 mm/s. The asymmetry in the magnitudes of u velocity components is due to the FS tool travel speed

Table 4

X-ray CT images of friction stir welds. (Darker regions are the discontinuities observed in welds).

Weld No.	Top View (at 0.5 mm from weld bottom)	Cross section	Side view (0.5 mm from weld centre in AS)
2 APR=0.2			
3 APR = 0.4			
4 APR = 0.6			
5 APR = 0.8			
6 APR = 1			

(V_T) along the same (x -) direction. The u velocity increases (along -ve x -direction) as the material reaches RS and decreases as it reaches the trailing edge. Further movement of material to AS leads to an increase in u velocity (along +ve x -direction), thereafter u velocity decreases towards the leading edge. The v velocity decreases as the material reaches RS, then material moves along -ve y -direction following the FS tool pro-

file. These trends are similar to the observations made by Arora et al. [23], based on a viscoplastic flow model.

The material flow model is used to calculate the strain rate, strain and flow stress around the pin per revolution. As depicted in Fig. 9, for an APR of 1 mm/rev, the equivalent strain rate and strain are the highest near FS tool pin. Further, for all the welds, the equivalent strain rate and

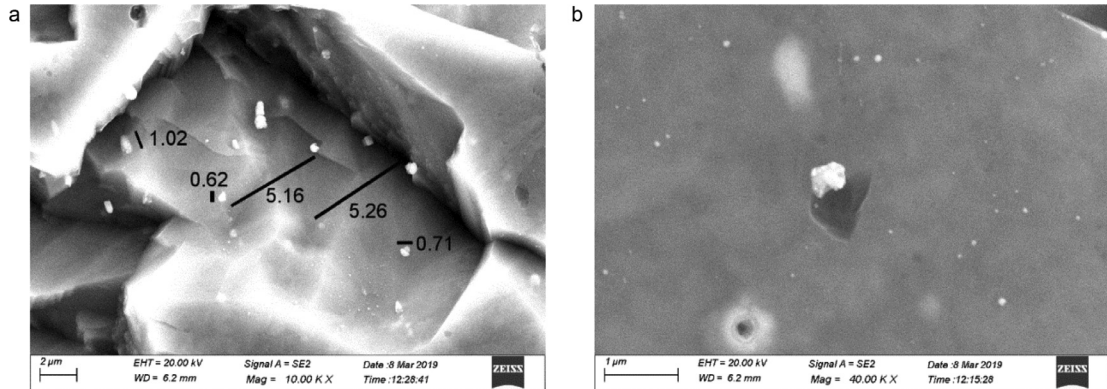
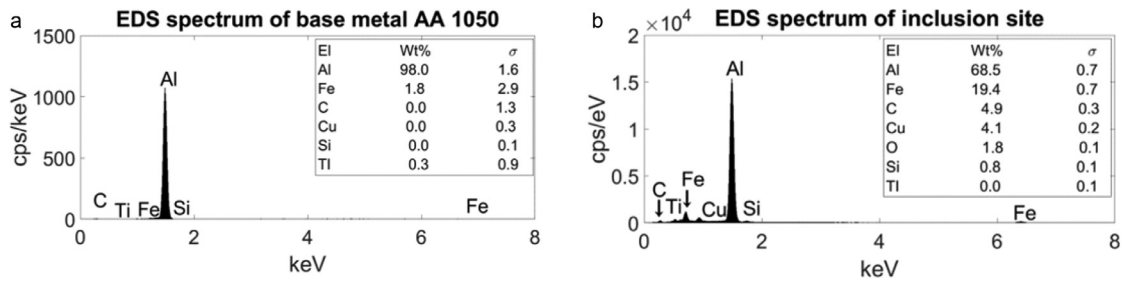
Fig. 4. (a) SEM of AA 1050 (distances in μm). 4(b) SEM of inclusion in AA 1050.

Fig. 5. (a) EDS of as received AA 1050. 5(b) EDS of inclusion in AA 1050.

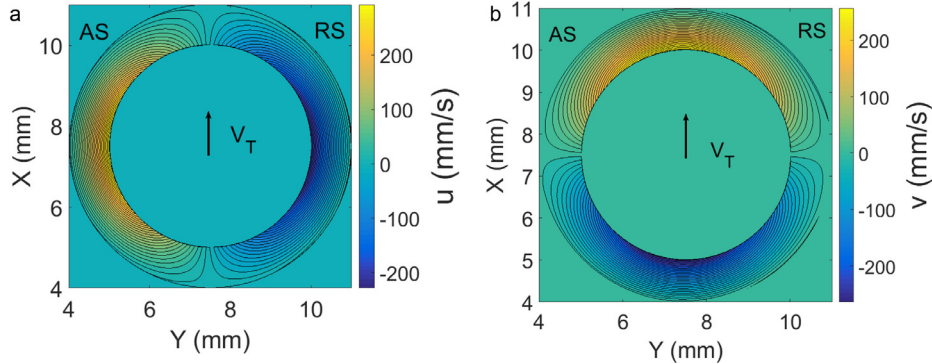
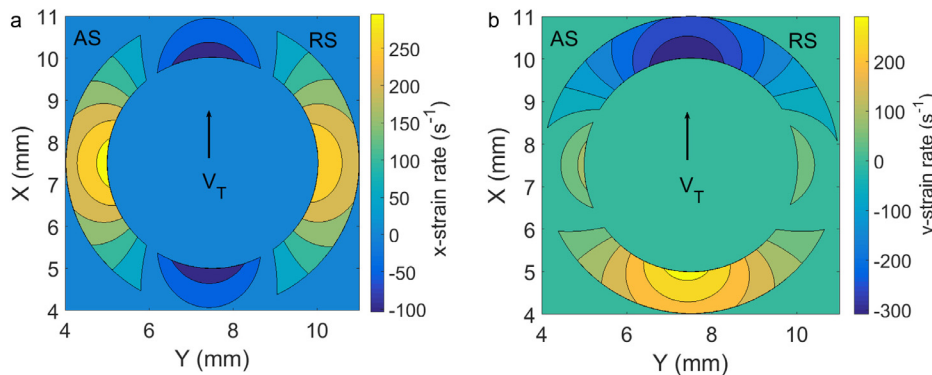
Fig. 6. (a). u velocity component in stir region (APR = 1 mm/rev). 6 (b). v velocity component in stir region (APR = 1 mm/rev).

Fig. 7. (a) X-direction strain rate distribution for pin-driven region at APR = 1 mm/rev. 7 (b) Y-direction strain rate distribution for pin-driven region at APR = 1 mm/rev.

equivalent strain at AS are nominally higher than RS. This is anticipated due to higher velocities at FS tool pin-workpiece interface at AS compared to RS. For APR = 1 mm/rev ($N = 1000$ RPM, $V_T = 1000$ mm/min), $\dot{\varepsilon}_x$ ranges from -104 to 321.6 s^{-1} and $\dot{\varepsilon}_y$ ranges from -309 to 309.8 s^{-1} (Fig. 7). Very similar ranges are estimated for the principal strain rates

($\dot{\varepsilon}_1$ from -104.8 to 322 s^{-1} , $\dot{\varepsilon}_2$ from $-309.8.8$ to 115.8 s^{-1}) while the equivalent strain rates $\dot{\varepsilon}_{eq}$ ranges from 144 to 230 s^{-1} (Fig. 9(a)). Similarly, the computed principal strains ε_1 and ε_2 range from -6.25 to 19.30 and -18.6 to 18.6 , respectively, while the equivalent strain ε_{eq} ranges from 8.7 to 13.8 (Fig. 9(b)). The computed strain and strain

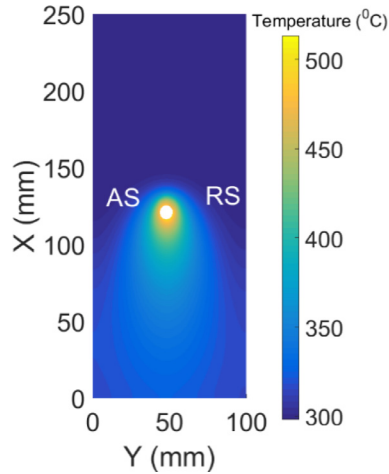


Fig. 8. Temperature distribution at APR = 1 mm/rev. (White region indicates the tool pin.).

rates are comparable to the previously reported works for Al alloys [4,5,23,24].

Fig. 7(a) and (b) show the contours of strain rates (along x and y directions, respectively) in the stir region, for APR of 1 mm/rev. The strain rate contours in the stir region is similar to the strain rate distribution estimated by Arora et al. [23]. The strain rates at the AS are higher than the RS due to the reason explained earlier. Fig. 8 shows the temperature contour around the FS tool pin, for representative APR of 1 mm/rev. The temperature in the stir region varied from 340 °C to 498 °C, with slightly higher temperatures at AS (498 °C) compared to RS (478 °C). The stir zone temperatures are used for the estimation of flow stresses (Pin-driven material flow model, Section 2.2). The thermal model (Section 2.1) was validated against the temperatures measured using thermocouples, in a previous work by the authors [66].

Fig. 10(a) and (b) show the variation of maximum equivalent strain rates and strain with APR respectively. Both the strain rate and strain decrease as the APR increases. This is due to a sharp drop in velocity gradients as the FS tool travel speed (V_T) increases, at constant FS tool rotation frequency. The constant FS tool rotation frequency dictates the same maximum tangential velocity at the FS tool pin. An increase of FS tool travel speed increases the width ($APR = V_T/N$) of the stir zone.

Fig. 11 shows the flow stress distribution around FS tool pin, void size upon nucleation & growth, and discontinuity upon cavity filling for APR of (a) 0.05; (b) 0.2; (c) 0.4; (d) 0.6; (e) 0.8 and (f) 1 mm/rev, respectively. Flow stress distribution is similar to equivalent strain and strain rate (Fig. 8(a) and (b)). Fig. 11(ii) (a)–(e) displays the void sizes upon nucleation & growth, and corresponding locations in the stir region, for

different APR conditions. These voids are opening almost all around the FS tool pin for all the APRs. This suggests that the stress and strain fields during FSW are sufficient for the nucleation and growth of voids at the inclusion sites. However, larger voids are formed at the Advancing side (AS), Retreating side (RS) and near the trailing and leading edges closer to the tool pin (Fig. 11(ii), yellow region). This was due to the higher strains (Fig. 9) and flow stress (Fig. 11) in these regions which lead to larger growth of voids (Eq. (22)). It was observed that for all APR, the size of voids (upon growth) exceeds the average $ipd/2$ of 2.6 μm in all the cases. This would lead to coalescence among neighboring voids and a cavity forms around the FS tool pin. Figs. 11 (iii) (a)–(e) shows the predicted morphology of the discontinuity (post cavity filling). The yellow region indicates the area which is filled by the incoming material and the blue region indicates the area which is left unfilled. Except for APR of 0.05 mm/rev, discontinuity is predicted for all other APR conditions. For all the cases with discontinuities, discontinuity area in AS is larger than RS. Further tunnel discontinuity is predicted by superimposing the discontinuities formed over successive FS tool rotations, which is shown in Fig. 12.

Fig. 12(a)–(f) shows the predicted morphology of the discontinuity over 20 mm long weld length, for different APR conditions. Fig. 12 suggests that the tunnel discontinuities are predicted on AS as well as RS, such that tunnel discontinuity at AS is larger than the RS. The tunnel discontinuity is observed only at the AS in the experiments. This is attributed to the simple velocity field assumed in the stir region.

Fig. 13(a) and (b) compare the experimentally observed and numerically predicted discontinuity volumes and areas, over 20 mm weld length. The experimental discontinuity volumes and areas are averaged over 3 welds and the error bars represent the standard deviation among the 3 welds, for each APR condition. Since the numerical model is two dimensional, the predicted discontinuity volume (Fig. 13(a)) is estimated by assuming that the discontinuity cross-section is same along the FS tool pin height. Similarly, the experimental CT is three dimensional, so maximum experimental discontinuity area (Fig. 13(b)) is measured at the horizontal plane ~0.5 mm above the weld bottom surface (Table 4). The numerical model over predicts the discontinuity volume. This is attributed to the lack of material flow model for the FS tool shoulder driven region. The presence of FS tool shoulder leads to higher homogeneous plastic deformation [7,64,65] and improved material flow, in the vicinity of the FS tool shoulder. This will increase the cavity filling and reduce the discontinuity size at the top of the stir region. This is evident from the experimental CT scans, as the discontinuity size increases from top to bottom in the stir region, for all the welds (Table 4, column 2). Further away (below) from the FS tool shoulder, the material would move primarily under the influence of the FS tool pin. Since only FS tool pin driven material is considered in this work, the stress and strain fields better represent the material movement at the weld bottom. The predicted discontinuity areas compare well against the maximum discontinuity areas (Fig. 13(b)).

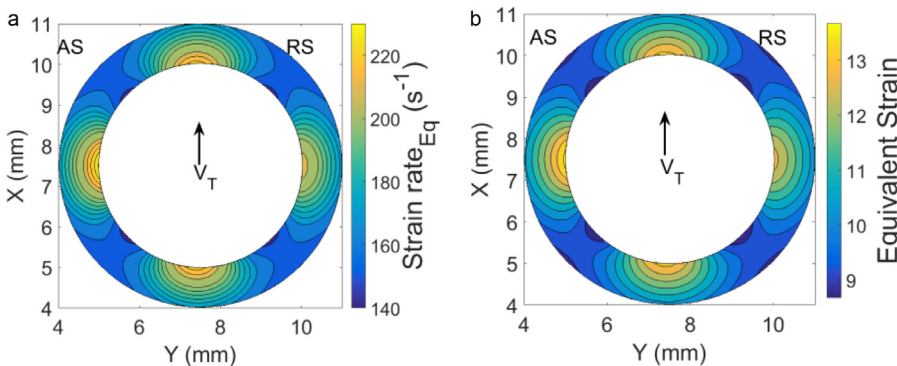


Fig. 9. (a) Equivalent strain rate distribution for pin-driven region at APR = 1 mm/rev. (b) Equivalent strain distribution for pin-driven region at APR = 1 mm/rev.

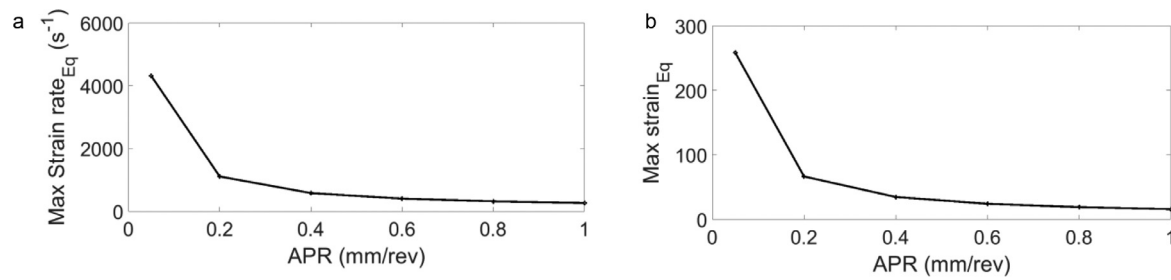


Fig. 10. (a) Maximum strain rate against APR in pin-driven region. 10 (b) Maximum strain against APR in pin-driven region.

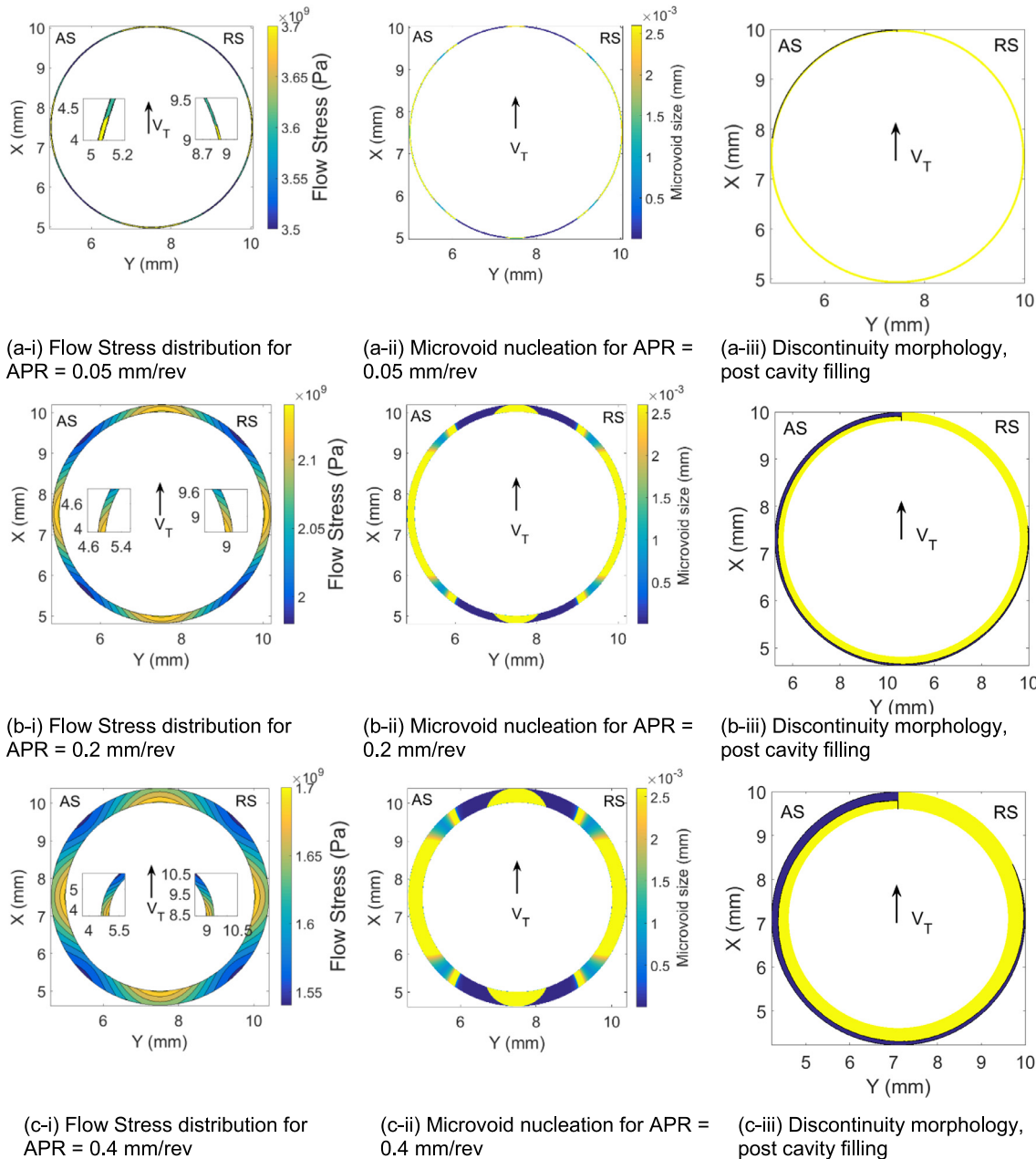


Fig. 11. Flow stress distribution, void size upon nucleation & growth, and discontinuity upon cavity filling for APR of (a) 0.05; (b) 0.2; (c) 0.4; (d) 0.6; (e) 0.8 and (f) 1 mm/rev, respectively (for pin driven material flow. (In figures iii (a-f), regions filled with material are in yellow and unfilled cavities are in blue.) (For interpretation of the references to colour in this figure legend, the reader is referred to the web version of this article.).

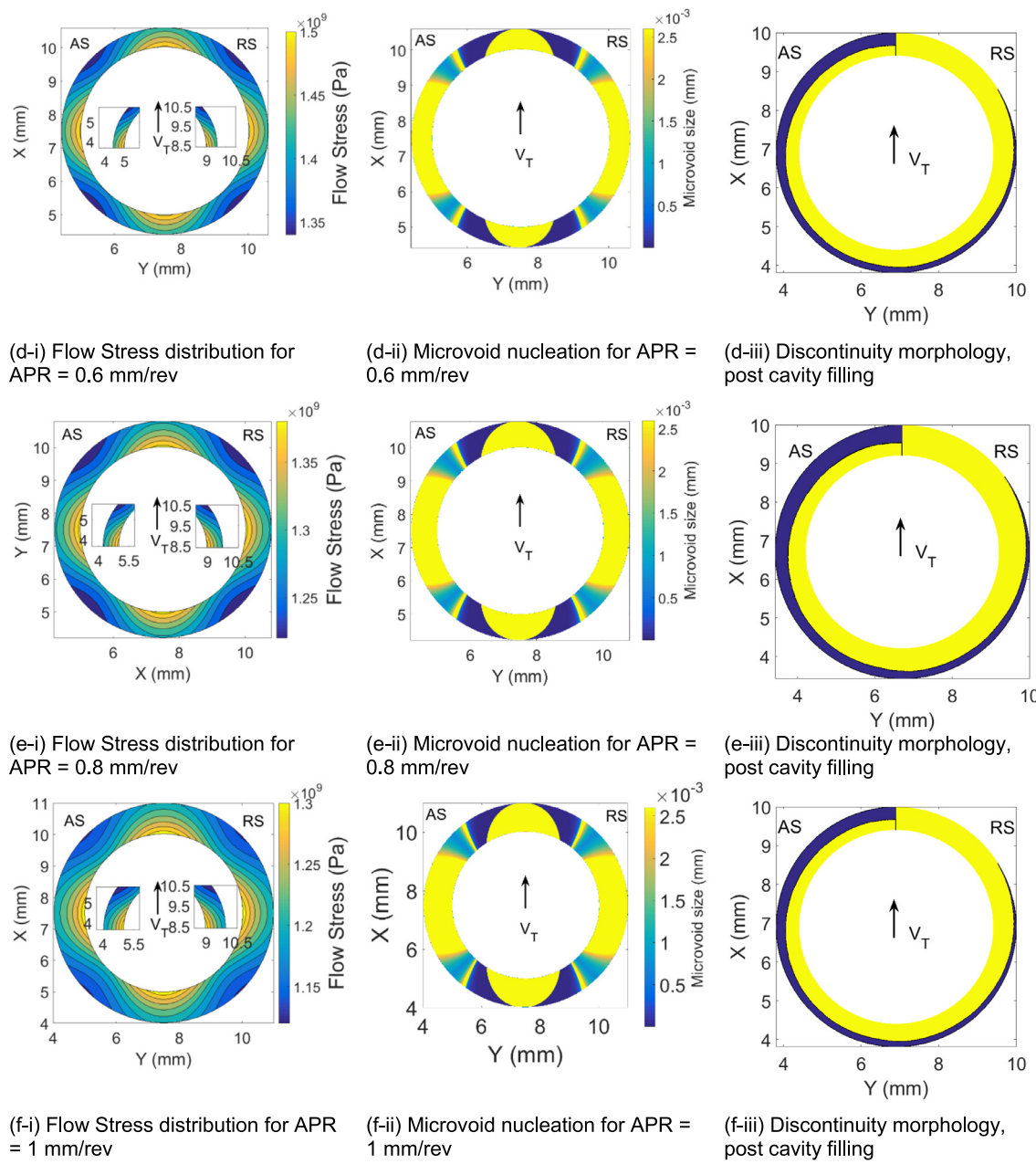


Fig. 11. Continued

5. Discussions

Many numerical and experimental studies have highlighted the significance of material movement towards joint formation during FSW. However, the nature of material movement (periodic or continuous) remains to be an open question. For periodic movement of material, a cavity must form around the FS tool pin, which should be filled during the process, for fully consolidated joint [12]. The plastic load limit model [49–54] sets the criteria for the formation of microvoids and growth, as a metal matrix with inclusions/second-phase particles is subjected to stress/strain. Therefore, the stress field plays a critical role in determining where the microvoids will nucleate in the stir region during FSW. The corresponding strain rate dictates the growth of the nucleated microvoids. For the representative case of AA 1050 in this study, the model predicts that the stress field and strain field magnitudes are sufficiently large to allow the microvoid nucleation (and growth) all around the FS tool during FSW (Figs. 8–11(i)). The microvoids grow to form

voids in the matrix. These voids grow large enough to coalesce with the neighboring voids and form a continuous annular cavity around the FS tool in stir region (Fig. 11(ii)). As the FS tool advances in travel direction, the incoming material at the leading edge moves around the FS tool from the retreating side, filling the annular cavity (Fig. 11 (iii), [1,2,5]). However, the incoming material also has a velocity profile such that the material moves fastest at the vicinity of FS tool pin and slows down to zero at the outer periphery of the stir region (Fig. 6, [5,19]). Thus the part of annular cavity close to the FS tool pin gets filled faster as compared to the areas close to the outer periphery of the stir region. This leads to the possibility that for relatively fast FS tool travel speeds, the annular cavity may not fill completely, leading to discontinuities in the friction stir welds (Fig. 12). This is very clearly observed from the experimental results (Table 4). As the FS tool travel speed is increased (for the same FS tool rotation frequency) across the experiments, larger discontinuities are formed in the friction stir welds (as observed in Fig. 11(ii), Fig. 13). Therefore, for a given material (flow

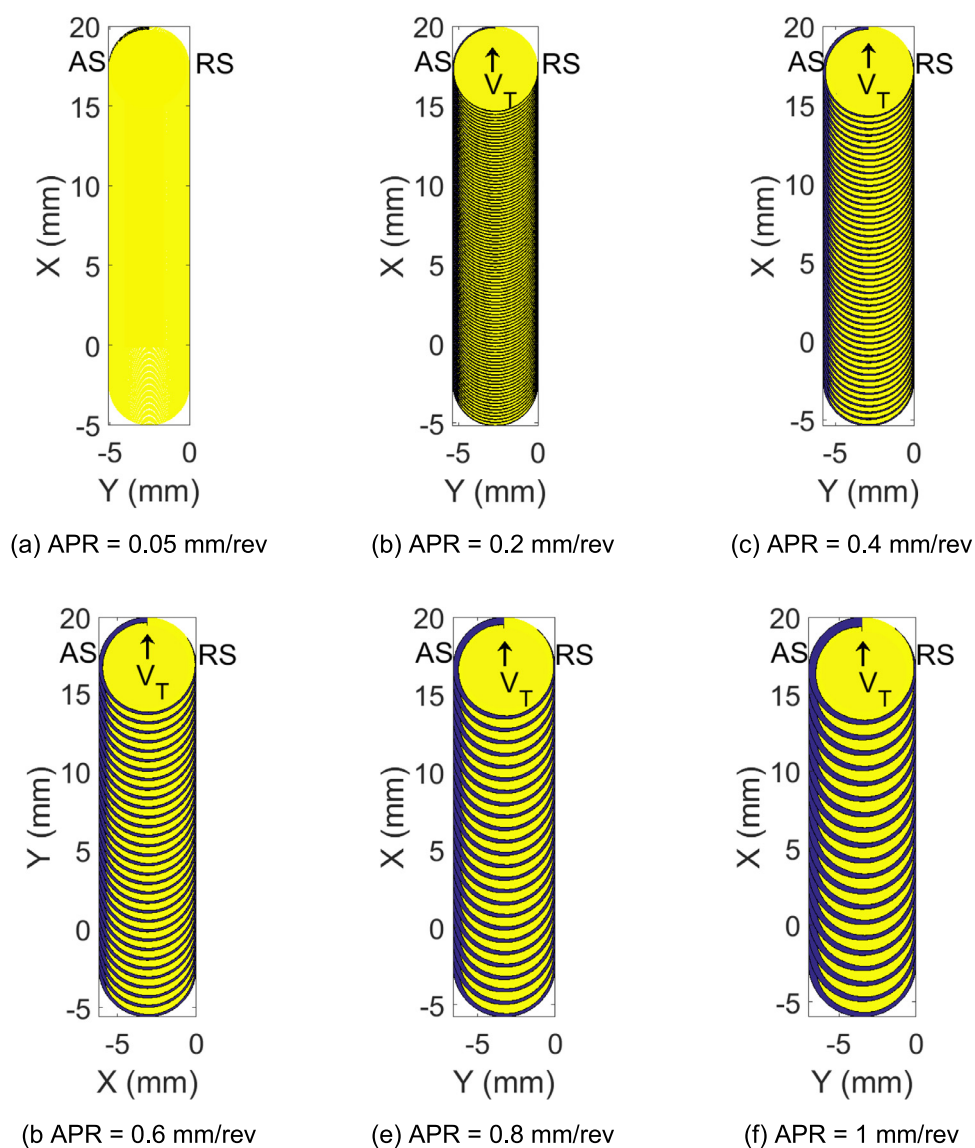


Fig. 12. Predicted tunnel discontinuity morphology for friction stir welds at different APR values. (Regions filled with material are in yellow and unfilled cavities are in blue.) (For interpretation of the references to colour in this figure legend, the reader is referred to the web version of this article.).

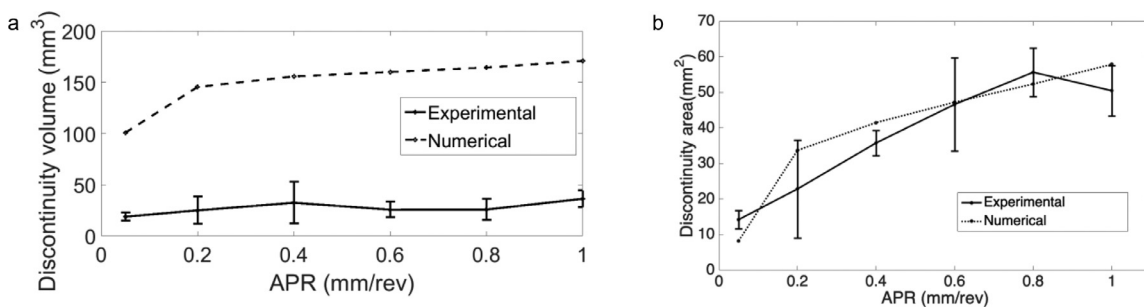


Fig. 13. (a) Experimental and numerical discontinuity volume over 20 mm weld sample. (b) Experimental and numerical discontinuity area for 20 mm weld sample.

characteristics at elevated temperature and strain during process), the FS tool travel speed should be such that the material velocity (provided by the FS tool rotation frequency) is sufficient for complete filling of the annular cavity. The ductile fracture (plastic load limit model) based analysis helps in understanding the cyclic nature of the material movement during FSW. The bulk material characteristics like mechanical and thermal properties (flow stress, thermal diffusivity, etc.) are known to

play a significant role during FSW. This work shows that the type, size and distribution of microstructural constituents like inclusions, second phase particles, precipitates, etc. also affect the joint formation during FSW.

The discontinuous periodic flow of material around the FS tool pin significantly influences the forces encountered during FSW/FSP [5,9,67–74]. The periodic material flow would lead to the periodicity

of forces. As the material offers resistance to the FSW tool motion along travel direction, the material is subjected to overall negative (opposite to travel direction) force (measured by dynamometer below workpiece [9,70–74]) along travel direction during FSW [72]. The magnitude of this force reduces as the cavity forms around the FSW tool, owing to the less resistance due to momentary shortage of material around FSW tool. The force magnitude will increase as the incoming material fills the cavity around the FSW tool. Since the cavity forms and gets filled once per FSW tool revolution, the forces along the travel direction also oscillate at the FSW tool rotation frequency. Once the cavity forms, there are minimum forces acting along the transverse direction (perpendicular to travel direction). As the incoming material fills the cavity, the material has to travel from leading edge and arrive at the retreating side (about $\pi/2$ radians of FSW tool rotation), for the forces to rise along the transverse direction. This explains a phase difference of $\pi/2$ between the forces along travel direction and transverse direction, which is observed in the previous works [9,71–72,74]. The transverse forces also oscillate at the tool rotation frequency due to cavity formation and its filling once per revolution. There is large compressive force along the FSW tool axis during FSW, due to the resistance offered by the material to the FSW tool's plunge into the material. The force along the FSW tool axis reduces as the cavity forms and the axial force increases as the incoming material fills the cavity. This makes the axial forces during FSW to oscillate at the FSW tool rotation frequency and in-phase with the forces along FSW tool travel direction. These observations are also reported earlier [9,68]. Thus, the formation of cavity and filling once per revolution provides explanations for the force (along travel, transverse & axial direction) oscillation characteristics, observed by many researchers.

6. Conclusions

To the author's knowledge, this is the first effort to capture the joint formation during FSW using a ductile fracture based criteria. During FSW, a stress based criteria is used to predict decohesion at the inclusions and matrix interface, in the stir region. A simple velocity field is assumed as first assumption, to model the strain, strain rate and stress field during the process. FSW of AA 1050 is performed with different process parameters and FSW samples are CT scanned to reveal the underlying discontinuities. The predicted discontinuity profiles and experimental discontinuity geometries are compared. This work shows that the sufficient magnitudes of stress and strain fields are available for nucleation, growth and coalescence of the voids during the process. This leads to the formation of an annular cavity in the stir region per revolution. The incoming material from the leading edge fills the cavity as it progresses to retreating side, trailing edge and advancing side. For some process parameters the cavity is not filled completely and leads to the formation of the discontinuities in the welded samples. Since the annular cavity is filled by the incoming material's movement around the FSW tool, the crescent shaped discontinuities are left in the stir region. For such cases, since the material moves from retreating side (RS) to the advancing side (AS), larger portion of the cavity is filled at the RS as compared to AS. As the FSW tool travel speed increases (for the same FSW tool rotation frequency), larger discontinuities are formed in the friction stir welds. The formation of tunnel discontinuity is captured by superpositioning of the discontinuities formed in consecutive passes along the feed direction. These geometric characteristics of the discontinuities captured by the numerical model compare well against the experimental observations from the post-weld CT scans. The major conclusions of this work are listed below:

1. During FSW, sufficient stress and strain levels are present for the nucleation, growth and coalescence, which lead to the formation of cavity around the FSW tool pin per revolution.
2. Formation of fully consolidated joint is subjected to the filling of this cavity.

3. This effort reveals and provides basis for the highly cyclic/periodic nature of the process.
4. The periodic formation and filling of the cavity would explain the force oscillations (along x, y & z direction) at the tool rotation frequency, observed by many researchers.
5. This understanding would be helpful towards developing strategies/methods for detecting and mitigating the discontinuities formed during FSW/FSP.

Declaration of Competing Interests

None.

Acknowledgment

The authors gratefully acknowledge the partial support of this work by the Science & Engineering Research Board, Department of Science & Technology, Government of India (File no. ECR/2017/000727/ES), Department of Mechanical Engineering, Microstructural Mechanics and Microforming Lab and Machine Tools Lab at Indian Institute of Technology Bombay, Mumbai. The authors would also like to thank Mr. Nikhil Gotawala and Mr. Abhishek Wadhigare for their help.

References

- [1] Colegrove PA, Shercliff HR. 3-Dimensional CFD modelling of flow round a threaded friction stir welding tool profile. Mater Process Technol 2005;169(2):320–7. doi:10.1179/136217104225021832.
- [2] Colligan K. Material flow behavior during friction welding of aluminum. Weld J 1999;75(7):229s–237s.
- [3] Williams S. Welding of airframes using friction stir. Air Space Eur 2001;3(3–4):64–6.
- [4] Colegrove PA, Shercliff HR, Zettler R. Model for predicting heat generation and temperature in friction stir welding from the material properties. Sci Technol Weld Join 2007;12(4):284–97.
- [5] Reynolds AP. Flow visualization and simulation in FSW. Scr Mater 2008;58(5):338–42.
- [6] Gratacap F, et al. Exploring material flow in friction stir welding: tool eccentricity and formation of banded structures. Int J Mater Form 2012;5(2):99–107.
- [7] Kumar KSVK, Kailas SV. The role of friction stir welding tool on material flow and weld formation. Mater Sci Eng A 2008;485(1–2):367–74. doi:10.1016/j.jmaa.2008.06.001.
- [8] Yan JH, Sutton MA, Reynolds AP. Processing and banding in AA2524 and AA2024 friction stir welding. Sci Technol Weld Join 2007;12(5):390–401.
- [9] Balasubramanian N, Mishra RS, Krishnamurthy K. Process forces during friction stir channeling in an aluminum alloy. J Mater Process Technol 2011;211(2):305–11.
- [10] Su H, Wu CS, Pittner A, Rethmeier M. Simultaneous measurement of tool torque, transverse force and axial force in friction stir welding. J Manuf Process 2013;15(4):495–500. doi:10.1016/j.jmapro.2013.09.001.
- [11] Astarita A, Squillace A, Carrino L. Experimental study of the forces acting on the tool in the friction-stir welding of AA 2024 T3 sheets. J Mater Eng Perform 2014;23(10):3754–61. doi:10.1007/s11665-014-1140-3.
- [12] Fonda R, et al. Material flow in friction stir welds. Metall Mater Trans A 2013;44(1):337–44.
- [13] Shah LH, Othman NH, Gerlich A. Review of research progress on aluminium-magnesium dissimilar friction stir welding. Sci Technol Weld Join 2018;23(3):256–70.
- [14] Tongne A, Desrayaud C, Jahazi Mohammad et Feulyarch, Eric. 2015. “Analytical modeling of material flow in friction stir welding”. In 11th International Seminar on Numerical Analysis of Weldability (Graz, Austria, Sept. 27–30, 2015). <http://espace2.etsmtl.ca/id/eprint/12991/>.
- [15] Boldsaikhan, E., D.A. Burford, and P. Gimenez. "Effect of plasticized material flow on the tool feedback forces during friction stir welding." Proc. Conf. On 'Friction stir welding and processing VI', San Francisco, CA, USA. 2011.
- [16] Boldsaikhan Enkhsaikhan, McCoy Michael. Analysis of tool feedback forces and material flow during friction stir welding. In: Friction stir welding and processing VII. Springer; 2013. p. 311–20. Cham.
- [17] Tan CW, et al. Microstructural evolution and mechanical properties of dissimilar Al–Cu joints produced by friction stir welding. Mater Des 2013;51:466–73.
- [18] Srivastava A, et al. Force measurement-based discontinuity detection during friction stir welding. J Manuf Process 2017;26:113–21.
- [19] He X, Gu F, Ball A. A review of numerical analysis of friction stir welding. Prog Mater Sci 2014;65:1–66.
- [20] Hamza E, Asim T, Mishra R. (2016) Computational Fluid Dynamics based Transient Thermal Analysis of Friction Stir Welding. In: 6th International and 43rd National Conference on Fluid Mechanics and Fluid Power, December 15–17, 2016, MNMITA, Allahabad, U.P., India. <http://eprints.hud.ac.uk/id/eprint/29395/>
- [21] Ma ZY, et al. Recent advances in friction stir welding/processing of aluminum alloys: microstructural evolution and mechanical properties. Crit Rev Solid State Mater Sci 2018;43(4):269–333.

- [22] Zhao Y, Han J, Domblesky JP, Yang Z, Li Z, Liu X. Investigation of void formation in friction stir welding of 7N01 aluminum alloy. *J Manuf Process* 2019;37:139–49. doi:[10.1002/nme.1620080411](https://doi.org/10.1002/nme.1620080411).
- [23] Arora A, Zhang Z, De A, DebRoy T. Strains and strain rates during friction stir welding. *Scr Mater* 2009;61(9):863–6. doi:[10.1016/j.scriptamat.2009.07.015](https://doi.org/10.1016/j.scriptamat.2009.07.015).
- [24] Fraser K, St-Georges L, Kiss LI. A mesh-free solid-mechanics approach for simulating the friction stir-welding process. In: *Join Technol IntechOpen* 2016.
- [25] Pan W, et al. A new smoothed particle hydrodynamics non-Newtonian model for friction stir welding: process modeling and simulation of microstructure evolution in a magnesium alloy. *Int J Plast* 2013;48:189–204.
- [26] Yong-Jai KWON, Seong-Beom SHIM, Dong-Hwan PARK. Friction stir welding of 5052 aluminum alloy plates. *Trans Nonferrous Metal Soc China* 2009;19:s23–7.
- [27] Arora A, et al. Torque, power requirement and stir zone geometry in friction stir welding through modeling and experiments. *Scri Mater* 2009;60(1):13–16.
- [28] Arora A, De A, DebRoy T. Toward optimum friction stir welding tool shoulder diameter. *Scri Mater* 2011;64(1):9–12.
- [29] Ulysse P. Three-dimensional modeling of the friction stir-welding process. *Int J Mach Tools Manuf* 2002;42(14):1549–57. doi:[10.1016/S0890-6955\(02\)00114-1](https://doi.org/10.1016/S0890-6955(02)00114-1).
- [30] Feulvach E, Roux J-C, Bergheau J-M. A simple and robust moving mesh technique for the finite element simulation of friction stir welding. *J Comput Appl Math* 2013;246:269–77.
- [31] Hamilton R, MacKenzie D, Li H. Multi-physics simulation of friction stir welding process. *Eng Comput* 2010;27(8):967–85.
- [32] Chen CM, Kovacevic R. Finite element modeling of friction stir welding—thermal and thermomechanical analysis. *Int J Mach Tools Manuf* 2003;43(13):1319–26.
- [33] Fratini L, Buffa G, Shivpuri R. Mechanical and metallurgical effects of in-process cooling during friction stir welding of AA7075-T6 butt joints. *Acta Mater* 2010;58(6):2056–67.
- [34] Chiumenti M, et al. Numerical modeling of friction stir welding processes. *Comput Methods Appl Mech Eng* 2013;254:353–69.
- [35] Van der Stelt AA, et al. Comparison of ALE finite element method and adaptive smoothed finite element method for the numerical simulation of friction stir welding AIP conference proceedings, 1353. AIP; 2011.
- [36] Simar A, et al. Integrated modeling of friction stir welding of 6xxx series Al alloys: process, microstructure and properties. *Prog Mater Sci* 2012;57(1):95–183.
- [37] Huang Y, et al. Numerical design of high depth-to-width ratio friction stir welding. *J Mater Process Technol* 2018;252:233–41.
- [38] Huang Y, et al. Joint formation mechanism of high depth-to-width ratio friction stir welding. *J Mater Sci Technol* 2019;35(7):1261–9.
- [39] Tutunchilar S, et al. Simulation of material flow in friction stir processing of a cast Al-Si alloy. *Mater Des* 2012;40:415–26.
- [40] Heurtier P, Jones MJ, Desrayaud C, Driver JH, et al. Mechanical and thermal modeling of friction stir welding. *J Mater Process Technol* 2006;171:348e57.
- [41] Cho HH, Hong ST, Roh JH, Choi HS, et al. Three-dimensional numerical and experimental investigation on friction stir welding processes of ferritic stainless steel. *Acta Mater* 2013;61:2649e61.
- [42] Bastier A, Maitournam MH, Roger F, Dang Van K. Modeling of the residual state of friction stir welded plates. *J Mater Process Technol* 2008;200:25e37.
- [43] Li Y, Luo M, Gerlach J, Wierzbicki T. Prediction of shear-induced fracture in sheet metal forming. *J Mater Process Technol* 2010;210(14):1858–69. doi:[10.1016/j.jmatprotec.2010.06.021](https://doi.org/10.1016/j.jmatprotec.2010.06.021).
- [44] Gorji MB, Mohr D. Predicting shear fracture of aluminum 6016-T4 during deep drawing: combining Yld-2000 plasticity with Hosford–Coulomb fracture model. *Int J Mech Sci* 2018;137:105–20. doi:[10.1016/j.ijmecsci.2018.01.008](https://doi.org/10.1016/j.ijmecsci.2018.01.008).
- [45] Shang X, Cui Z, Fu MW. A ductile fracture model considering stress state and Zener–Hollomon parameter for hot deformation of metallic materials. *Int J Mech Sci* 2018;144:800–12. doi:[10.1016/j.ijmecsci.2018.06.030](https://doi.org/10.1016/j.ijmecsci.2018.06.030).
- [46] Su H, et al. Thermal energy generation and distribution in friction stir welding of aluminum alloys. *Energy* 2014;77:720–31.
- [47] G.R. Johnson and W.H. Cook, “A constitutive model and data for metals subjected to large strains, high strain rates and high temperatures,” in Proceedings of the 7th International Symposium on Ballistic, p. 541, The Hague, The Netherlands, 1983.
- [48] Reddy ACHENNAKESAVA. Formability of warm deep drawing process for AA1050-H18 rectangular cups. *Int J Mech Prod Eng Res Dev* 2015;5(4):85–97.
- [49] Argon AS, Im J. Separation of second phase particles in spheroidized 1045 steel, Cu-0.6 pct Cr alloy, and maraging steel in plastic straining. *Metall Trans A* 1975;6(4):839.
- [50] McClintock FA. A criterion for ductile fracture by the growth of holes. *J Appl Mech* 1968;35(2):363–71.
- [51] Bandstra JP, Koss DA. Modeling the ductile fracture process of void coalescence by void-sheet formation. *Mater Sci Eng A* 2001;319:490–5.
- [52] Reddy AC, Sundar Rajan S. Influence of ageing, inclusions and voids on ductile fracture mechanism in commercial Al-alloys. *Bull Mater Sci* 2005;28(1):75–9.
- [53] Huber G, Brechet Y, Pardoën T. Predictive model for void nucleation and void growth controlled ductility in quasi-eutectic cast aluminium alloys. *Acta Mater* 2005;53(9):2739–49.
- [54] Argon AS, Im J, Safoglu R. Cavity formation from inclusions in ductile fracture. *Metall Trans A* 1975;6(4):825.
- [55] Argon AS. Formation of cavities from nondeformable second-phase particles in low temperature ductile fracture. *J Eng Mater Technol* 1976;98(1):60–8.
- [56] McClintock F, Kaplan SM, Berg CA. Ductile fracture by hole growth in shear bands. *Int J Fract Mech* 1966;2(4):614–27.
- [57] Rice JR, Tracey DM. On the ductile enlargement of voids in triaxial stress fields*. *J Mech Phys Solids* 1969;17(3):201–17. doi:[10.1016/0022-5096\(69\)90033-7](https://doi.org/10.1016/0022-5096(69)90033-7).
- [58] Hill Rodney. *The mathematical theory of plasticity* 1998;11.
- [59] Villuendas A, Roca A, Jorba J. Change of young's modulus of cold-deformed aluminum AA 1050 and of AA 2024 (T65): a comparative study. *Mater Sci Forum*, 539; 2007. Trans Tech Publications.
- [60] Hallberg H. Influence of process parameters on grain refinement in AA1050 aluminum during cold rolling. *Int J Mech Sci* 2013;66:260–72.
- [61] Gashti SO, et al. Effects of grain size and dislocation density on strain hardening behavior of ultrafine grained AA1050 processed by accumulative roll bonding. *J Alloys Compd* 2016;658:854–61.
- [62] Martinsen Vegard. Micromechanical modelling of strain localization and fracture in aluminium 2012 MS thesis.
- [63] Jariyaboon M, et al. The effect of atmospheric corona treatment on AA1050 aluminum. *Corros Sci* 2010;52(6):2155–63.
- [64] Leal RM, et al. Material flow in heterogeneous friction stir welding of thin aluminium sheets: effect of shoulder geometry. *Mater Sci Eng A* 2008;498(1–2):384–91.
- [65] Uygur I. Influence of shoulder diameter on mechanical response and microstructure of FSW welded 1050 Al-alloy. *Arch Metall Mater* 2012;57(1):53–60.
- [66] Gotawala Nikhil, Shrivastava Amber. Investigation of interfacial diffusion during dissimilar friction stir welding. In: *Friction stir welding and processing X*. Springer; 2019. p. 109–19. Cham.
- [67] Xiong JT, et al. Characterisation of periodic variation in torque occurred in friction stir welding process. *Sci Technol Weld Join* 2014;19(4):350–4.
- [68] Qian JW, et al. Periodic variation of torque and its relations to interfacial sticking and slipping during friction stir welding. *Sci Technol Weld Join* 2012;17(4):338–41.
- [69] Mehta M, Chatterjee K, De A. Monitoring torque and traverse force in friction stir welding from input electrical signatures of driving motors. *Sci Technol Weld Join* 2013;18(3):191–7.
- [70] Dialami N, et al. A fast and accurate two-stage strategy to evaluate the effect of the pin tool profile on metal flow, torque and forces in friction stir welding. *Int J Mech Sci* 2017;122:215–27.
- [71] Longhurst WR, et al. Torque control of friction stir welding for manufacturing and automation. *Int J Adv Manuf Technol* 2010;51(9–12):905–13.
- [72] Rodriguez J, Ramirez AJ. Friction stir welding of mild steel to alloy 625—development of welding parameters. *Sci Technol Weld Join* 2014;19(4):343–9.
- [73] Firouzdar V, Kou S. Al-to-Mg friction stir welding: effect of material position, travel speed, and rotation speed. *Metal Mater Trans A* 2010;41(11):2914–35.
- [74] Balasubramanian N, Gattu B, Mishra RS. Process forces during friction stir welding of aluminium alloys. *Sci Technol Weld Join* 2009;14(2):141–5.